Acta Pharmaceutica Sinica B 2024;14(6):2748–2760

Chinese Pharmaceutical Association
Institute of Materia Medica, Chinese Academy of Medical Sciences

Acta Pharmaceutica Sinica B

www.elsevier.com/locate/apsb
www.sciencedirect.com

ORIGINAL ARTICLE

Cisplatin-based miRNA delivery strategy inspired by the circCPNE1/miR-330-3p pathway for oral squamous cell carcinoma

Hua-yang Fan[a,†], Ming-da Zhao[b,†], Hong-jie Jiang[c], Zhen-wei Yu[a], Yu-jiang Fan[b], Xin-hua Liang[a,*], Ya-ling Tang[c,*], Yong Sun[b,*]

[a]*State Key Laboratory of Oral Diseases & National Center for Stomatology & National Clinical Research Center for Oral Diseases & Department of Oral and Maxillofacial Surgery, West China Hospital of Stomatology, Sichuan University, Chengdu 610041, China*
[b]*National Engineering Research Center for Biomaterials, Sichuan University, Chengdu 610065, China*
[c]*State Key Laboratory of Oral Diseases & National Center for Stomatology & National Clinical Research Center for Oral Diseases & Department of Oral Pathology, West China Hospital of Stomatology, Sichuan University, Chengdu 610041, China*

Received 11 September 2023; received in revised form 8 November 2023; accepted 14 December 2023

KEY WORDS

Oral squamous cell carcinoma;
CircRNA;
MiRNA sponge;
Antagomir;
MiRNA delivery;
Cisplatin-based nanoparticles;
Drug delivery systems;
Tumor elimination

Abstract Circular RNAs (circRNAs) are ideal biomarkers of oral squamous cell carcinoma (OSCC) because of their highly stable closed-loop structure, and they can act as microRNA (miRNA) sponges to regulate OSCC progression. By analyzing clinical samples, we identified circCPNE1, a dysregulated circRNA in OSCC, and its expression level was negatively correlated with the clinical stage of OSCC patients. Gain-of-function assays revealed the tumor-suppressive effect of circCPNE1, which was then identified as a miR-330-3p sponge. MiR-330-3p was recognized as a tumor promoter in multiple studies, consistent with our finding that it could promote the proliferation, migration, and invasion of OSCC cells. These results indicated that selective inhibition of miR-330-3p could be an effective strategy to inhibit OSCC progression. Therefore, we designed cationic polylysine-cisplatin prodrugs to deliver antago-miR-330-3p (a miRNA inhibitory analog) *via* electrostatic interactions to form PP@miR nanoparticles (NPs). Paratumoral administration results revealed that PP@miR NPs effectively inhibited subcutaneous tumor progression and achieved partial tumor elimination (2/5), which confirmed the critical role of miR-330-3p in OSCC development. These findings provide a new perspective for the development of OSCC treatments.

*Corresponding authors.
E-mail addresses: lxh88866@scu.edu.cn (Xin-hua Liang), tangyaling@scu.edu.cn (Ya-ling Tang), sunyong8702@scu.edu.cn (Yong Sun).
[†]These authors made equal contributions to this work.
Peer review under the responsibility of Chinese Pharmaceutical Association and Institute of Materia Medica, Chinese Academy of Medical Sciences.

https://doi.org/10.1016/j.apsb.2024.02.009
2211-3835 © 2024 The Authors. Published by Elsevier B.V. on behalf of Chinese Pharmaceutical Association and Institute of Materia Medica, Chinese Academy of Medical Sciences. This is an open access article under the CC BY-NC-ND license (http://creativecommons.org/licenses/by-nc-nd/4.0/).

© 2024 The Authors. Published by Elsevier B.V. on behalf of Chinese Pharmaceutical Association and Institute of Materia Medica, Chinese Academy of Medical Sciences. This is an open access article under the CC BY-NC-ND license (http://creativecommons.org/licenses/by-nc-nd/4.0/).

1. Introduction

CircRNAs are a subclass of non-coding RNAs (ncRNAs). They have a covalent closed-loop structure without a 5′ cap and a 3′ polyadenylate tail; these characteristics make circRNAs highly stable and are therefore considered to be ideal tumor-associated biomarkers[1]. In addition, mounting studies have shown that circRNAs significantly impact the development of OSCC[2]. CircRNA can competitively bind miRNAs (acting as a miRNA sponge) and deregulate miRNA repression of downstream genes related to tumor progression[3]. A previous study found that circIGHG regulated *IGF2BP3* expression by sponging miR-142−5p, which promoted the epithelial−mesenchymal transition (EMT) and consequently enhanced OSCC cell invasion[4]. Many studies have investigated the regulatory role of the circRNA/miRNA axis in OSCC, but relevant therapeutic strategies are scarce[5]. Since circRNAs are ideal biomarkers, tumor-associated signaling pathways tracked by circRNAs may be promising therapeutic targets.

miRNA is an important target in RNA interference (RNAi) strategies, and specific inhibition of tumor-promoting miRNAs is an effective cancer treatment approach[6]. Researchers have identified numerous miRNAs involved in regulating OSCC progression that affected cell proliferation, apoptosis, metastasis, and drug resistance[7], but few studies focused on therapeutic miRNA delivery strategies. Several miRNA-based therapies have been developed and entered clinical trials, including miR-155 (closely related to the pathogenesis of lymphoma) and its inhibitor MRG-106, which was well tolerated and clinically active in phase I clinical trials[8]. Miravirsen, a miR-122 inhibitor designed to treat hepatitis C infection, has also entered clinical trials[9]. These studies demonstrated the great therapeutic potential of inhibiting targeted miRNAs. Antagomirs are cholesterol-binding single-stranded RNA analogs that can complement miRNAs, specifically inhibiting endogenous miRNA levels[10]. NPs-based drug delivery systems (DDSs) incorporating antagomirs can target tumor tissue and have few side effects. For example, lipid nanoparticles (LNPs) loaded with specific antagomirs were found to suppress murine tumors[11]. Moreover, nanoparticle delivery systems can combine miRNA therapy with chemotherapy to provide synergistic benefits[12,13].

Chemotherapy is the conventional treatment for OSCC, and cisplatin is the first-line chemotherapeutic agent whose main limitations are long-term drug resistance and inevitable systemic toxicity[14,15]. One of the recognized mechanisms of cisplatin resistance is hindered drug transport[16]. Topical delivery of cisplatin nanomedicines was found to promote cisplatin accumulation and retention in cancer cells with reduced systemic toxicity[17]. Importantly, it was found that localized delivery of cisplatin has the potential to "intercept" cancer development, thereby preventing the emergence of fully developed OSCC with multiple resistance mechanisms[18]. A phase I/II study of PRV 111 (a transmucosal cisplatin delivery system) in 10 subjects with OSCC demonstrated a response rate of over 87%, tumor reduction of over 70% within 7 days, and no systemic toxicity[19]. Recently, the effects of cisplatin on the tumor microenvironment (TME) have been widely studied, leading to a growing interest in the development of DDSs that improve the efficacy and safety of cisplatin[20]. The use of platinum-based NPs is surprisingly scarce among various platinum formulations (*e.g.*, lipoplatin, NPs composed of lipids and cisplatin). Nevertheless, platinum-based NPs have gained attention in recent years for their use as delivery platforms in combination with other cancer therapies[21]. The success of these DDSs depends on their ability to overcome challenges in cancer development, such as tumor heterogeneity and drug resistance[22]. Notably, nanocarriers loaded with miRNAs and cisplatin have the potential to reverse drug resistance by the effect of miRNAs, thereby improving therapeutic efficacy[23].

In this study, we investigated the circCPNE1/miR-330-3p signaling axis involved in the regulation of OSCC progression through *in vitro* and *in vivo* experiments. Previous studies have identified miR-330-3p as a critical protumor factor[24], thus interventions targeting this miRNA may be an effective strategy for treating OSCC. Here, we hypothesized that a delivery system combining the miR-330-3p inhibitor with cisplatin would rapidly "intercept" the development of OSCC and eliminate tumor tissue *in vivo*. Therefore, we prepared a cationic polylysine-modified cisplatin prodrug and combined it with antagomiR-330-3p to form PP@miR NPs. The antitumor effects of PP@miR NPs were validated by a subcutaneous xenograft tumor model in nude mice. In brief, we successfully developed a therapeutic strategy for OSCC based on the circCPNE1/miR-330-3p pathway.

2. Materials and methods

2.1. Patients and specimens

Human specimens were obtained from patients who gave informed consent under protocols approved by the Institutional Ethics Committee of West China Hospital of Stomatology of Sichuan University (approval no. WCHSIRB-CT-2021-524). We included 33 pairs of OSCC and para-cancerous specimens from patients between 2019 and 2021 at the Department of Oral Pathology, West China Hospital of Stomatology of Sichuan University. The clinicopathological features of these OSCC patients are shown in Supporting Information Table S1.

2.2. Cell lines and cell culture

Human OSCC cell lines (CAL27, HSC2, and Cal33) and normal oral keratinocytes (NOK) were obtained from the State Key Laboratory of Oral Diseases of Sichuan University. CAL27, HSC2, and Cal33 cells were cultured in Dulbecco's modified Eagle medium (DMEM; Gibco, MA, USA). NOK cells were cultured in a Keratinocyte serum-free medium (K-SFM; Gibco, MA, USA). The media were supplemented with 10% fetal bovine serum (FBS; Gibco, MA, USA). The cells were maintained at 37 °C with 5% CO_2 atmosphere.

2.3. RNA extraction and real-time quantitative PCR (qRT-PCR)

Total RNA was extracted using TRIzol reagent (TaKaRa, Kyoto, Japan) and according to its instructions. First-strand cDNA for mRNA was generated by PrimeScript RT reagent Kit (TaKaRa, Kyoto, Japan), and first-strand cDNA for miRNA was generated by miRNA First-Strand cDNA Synthesis Kit (Sangon, Shanghai, China), followed by qRT-PCR carried out with SYBR Green Master Mix (Gibco, MA, USA). The PCR primers were designed and synthesized by Sangon Biotech (Shanghai, China) and are listed in Supporting Information Table S2.

2.4. Ribonuclease R (RNase R) treatment

The total RNA of OSCC cells was extracted with TRIzol reagent (TaKaRa) and then treated according to RNase R kit (Geneseed, Canton, China) instructions. Each 2.5 μg of RNA was incubated with l0 U RNase R and then 37 °C for 30 min, followed by 70 °C for 10 min qRT-PCR was then performed to analyze the expression levels of the treated RNA.

2.5. Fluorescent in situ hybridization (FISH)

FISH experiments were performed according to the instructions of the FISH kit for paraffin sections and cells (Genepharma, Shanghai, China). Genepharma designed fluorescent probes against circCPNE1, miR-330-3p, and 18S RNA. Images were captured by the fluorescence microscope (Olympus BX51, Tokyo, Japan).

2.6. Nucleocytoplasmic segregation assay

Cytoplasmic and nuclear RNA fractions were extracted according to the instructions of the nucleocytoplasmic segregation kit (BestBio, Shanghai, China) and subsequently analyzed by qRT-PCR. *U6* and *GAPDH* were used as nuclear and cytoplasmic controls, respectively.

2.7. Cell transfection

Cas9X™ (Soochow, China) designed and provided plasmids and transposon vectors for overexpression of circCPNE1, and constructed Cal27 cells stably overexpressing circCPNE1. GenePharma designed and provided the miR-330-3p mimics and negative controls (NC). Cell transfection was performed according to the Endofectin-Max reagent (GeneCopoeia, MD, USA) instructions.

2.8. Cell counting kit-8 (CCK-8) assay

Treated cells were seeded in 96-well plates at a density of 2×10^3 cells per well and cultured for 1−4 days. Subsequently, 10 μL of CCK-8 reaction solution (Dojindo, Shanghai, China) was added to 100 μL of serum-free medium and incubated at 37 °C for 1 h. Then, the optical density (OD) values at 450 nm were measured using a microplate reader (Thermo Scientific, CA, USA).

2.9. Wound healing assay

Treated cells were seeded in 6-well plates at a density of 4×10^5 cells per well and cultured to confluency. Then, tumor cells were scraped with a P200 tip at 0 h, washed with phosphate-buffered saline (PBS), and cultured with a serum-free medium. At least three nonoverlapping field images were obtained under phase-contrast microscopy at 24 h. The area of closed scratches was calculated using ImageJ (NIH, USA) software.

2.10. Transwell invasion assay

Transwell invasion assay was performed using 24-well Transwell chambers (pore size = 8 μm) coated with Matrigel (Corning, AZ, USA). A total of 200 μL of cell suspension in serum-free medium was added to the upper chamber, and 600 μL of 10% FBS medium was added to the lower chamber. After 36−48 h of incubation, the cells were fixed with 4% paraformaldehyde for 20 min and stained with 1% crystal violet for 20 min. The number of stained cells was counted using a random selection of five areas under phase-contrast microscopy.

2.11. RNA immunoprecipitation (RIP) assay

After cell lysis with RIP lysate, 100 μL of lysate was mixed with washed magnetic beads, then conjugated with human anti-AGO2 antibody (Proteintech, IL, USA) and rabbit IgG (Proteintech, IL, USA), placed in a room at 4 °C and rotated overnight. At last, the magnetic beads were collected, and the target RNA was extracted and purified for detection by qRT-PCR assay.

2.12. Western blotting

OSCC cells were harvested in RIPA buffer (Sangon, Shanghai, China). Protein concentrations were determined using the BCA protein assay kit (Beyotime, Shanghai, China). The separation of proteins was performed on a 10% SDS-PAGE gel (Bio-Rad, CA, USA) at 80−120 V. The resolved proteins were then transferred to a nitrocellulose membrane (Bio-Rad, CA, USA) and incubated with a primary antibody followed by a horseradish peroxidase-conjugated secondary antibody (Abcam, MA, USA). Antibodies used in this study include anti-GAPDH antibody (Abcam, MA, USA), anti-SOX6 antibody (Proteintech, IL, USA), anti-ERBB4 antibody (Proteintech, IL, USA), anti-AKT antibody (Abmart, Shanghai, China), and anti-Bcl2 antibody (Abmart, Shanghai, China). The blots were visualized using the ChemiDoc™ XRS+ System (Bio-Rad, CA, USA). Quantification of Western blot bands was calculated by ImageJ, and the expression level quantitation value is the ratio of the gray value of the target band to the corresponding GAPDH gray value.

2.13. Dual-luciferase reporter assay

The wild and mutant types of luciferase vectors for circCPNE1 and *SOX6* were constructed by Genechem (Shanghai, China). Transfected cells were tested for luciferase using a dual luciferase reporter kit (Yeasen, Shanghai, China).

2.14. Preparation and characterization of Pt (IV)−PLys (PP)

The method was based on that previously reported by our group with minor modifications[25]. Firstly, 200 mg of cisplatin (Aladdin, Shanghai, China) was dispersed in 5 mL of ultrapure water, and ultrasound for 10 min, then, 1 mL of H2O2 (30%) was added and reacted for 2 h at 50 °C. The above suspension was kept at 4 °C overnight, and the hydroxy-modified cisplatin was obtained by

centrifugation and vacuum drying. Then, 66.8 mg of hydroxy-modified cisplatin was dispersed in 6 mL of dimethyl sulfoxide (DMSO), and 40 mg of succinic anhydride was added and kept dark at room temperature for 12 h. The suspension became clear and transparent, 152.8 mg of 1-(3-dimethylaminopropyl)-3-ethylcarbodiimide (EDC) and 92 mg of *N*-hydroxy succinimide (NHS) in 0.5 mL of DMSO were added into the above solution for 1 h to activate the carboxyl group. Then, 1.2 g of ε-PLys (Aladdin, Shanghai, China) was dissolved into 5 mL of a mixture of DMSO and ultrapure water (3:2, *v*/*v*), and added to the above solution. After 12 h, the resulting solution was dialyzed against PBS (molecular weight cutoff = 3500) for 3 days and concentrated in an ultrafiltration tube to obtain the PP solution. The concentration of Pt was determined by ion-pair chromatography (IPC). The characteristic of chemical bonding of PP was detected by Fourier transform infrared spectroscopy (FTIR) and 1H NMR. Matrix-assisted laser desorption/ionization time-of-flight (MALDI−TOF) was used to determine the molecular weight of PP.

2.15. Preparation and characterization of PP@miR NPs

A certain amount of PP solution was mixed with antagomir (Genepharma, Shanghai, China) and quickly vortexed to obtain PP@miR NPs. Antagomir-NC was used as the control group to prepare PP@miR-NC NPs. NPs with different Pt and antagomir ratios were prepared, and the loading of antagomir was examined by gel electrophoresis. Dynamic light scattering (DLS) was used to measure the particle size and surface potential of PP@miR NPs at different Pt/antagomir ratios. To test the reduction responsiveness of the NPs, PP@miR NPs were dispersed in PBS solution or PBS containing 10 mmol/L glutathione (GSH), and the particle size and the size distribution (polydispersity index, PDI) of PP@miR NPs were measured by DLS at different time points. Transmission electron microscopy (TEM) was used to observe the morphology of PP@miR NPs and the morphology after GSH treatment. For the release profile of antagomir, PP@miR-Cy3 NPs were dispersed in PBS solution or PBS containing 10 mmol/L GSH, at predetermined time points, the nanoparticles were precipitated by centrifugation at 13,000 rpm for 30 min (MIULAB, Hangzhou, China), and the supernatant was removed and examined by multifunctional microporous plate detector (H1M, BioTek, CA, USA) in a 96-well plate.

2.16. Cellular uptake

Cal27 cells were seeded in 12-well plates at a density of 2×10^5 cells per well and cultured overnight. After incubation with PP@miR-Cy3 NPs and antagomir-Cy3 for 4 h, cells were fixed with 4% paraformaldehyde for 15 min. The cells were then washed with PBS and the nuclei were stained with DAPI (Vector, CA, USA) for 15 min. Images were captured by the fluorescence microscope (Olympus BX51).

2.17. Animal experiments

Five-week-old female BALB/c nude mice were purchased from HFK Bioscience (Peking, China), and they were fed under standard pathogen-free conditions. OSCC cells (3×10^6) were injected subcutaneously into the mice to form tumors for subsequent experiments. *In vivo* biodistribution experiments: solutions of PP@miR-Cy3 NPs and antagomir-Cy3 were injected adjacent to the tumor; an *in vivo* imaging system (IVIS) was used to measure bioluminescence in the tumor at 0, 6, and 12 h, respectively; the heart, liver, spleen, lungs, and kidneys were collected and measured for bioluminescence after 12 h. *In vivo* effects of PP@miR NPs: the drugs were injected every other day as scheduled, and finally the mice were sacrificed and tumors were dissected, which were weighed and photographed to calculate the tumor volume according to Eq. (1):

$$\text{Volume} = 1/2 \times \text{Length} \times \text{Width}^2 \quad (1)$$

Tumor tissue was excised for further testing. The heart, liver, spleen, lungs, and kidneys were removed to determine the biosafety of the drug. All experimental procedures were executed according to the protocols approved by the Institutional Ethics Committee of West China Hospital of Stomatology of Sichuan University (approval no. WCHSIRB-D-2021-584).

2.18. Immunohistochemistry (IHC) and terminal deoxynucleotidyl transferase dUTP nick end labeling (TUNEL) assay

IHC staining was performed under the manufacturers' instructions (Beyotime, Shanghai, China). The first antibodies include SOX6 (Proteintech, IL, USA), KI67 (Cell Signaling Technology, MA, USA), and CD31 (Abcam, MA, USA). Sections were scanned using the Aperio Imagescope digital pathology system (Leica, Wetzlar, Germany). Three 200 × fields of view were randomly selected for each section, and the intensity of SOX6 and Ki67 staining and the number of positive cells were evaluated and calculated independently by two pathologists. The staining intensity could be divided into 4 grades according to the staining intensity: − (0 score), + (1 score), ++ (2 score), and ++++ (3 score). The number of stained cells can be divided into 4 grades: negative (number of positive cells <5%, 0 score), weakly positive (5% ≤ number of positive cells <25%, 1 score), moderately positive (25% ≤ number of positive cells <50%, 2 score), strongly positive (50% ≤ number of positive cells, 3 score). The sum of the staining intensity and the number of stained cells scores of SOX6 in each field of view were counted, and then the average of the scores was calculated for each specimen. TUNEL assay was performed under the manufacturer's instructions (Promega, WI, USA).

2.19. Statistical analysis

Results were presented as mean ± standard deviation (SD) and were analyzed and presented by GraphPad Prism 9 (MA, USA). Correlations were analyzed using the χ^2 test. Means comparisons were performed using Student's *t*-test or one-way ANOVA. $P < 0.05$ was statistically significant.

3. Results

3.1. Characterization of circCPNE1 and its function in inhibiting OSCC progression in vitro and in vivo

In our previous study, we investigated the expression levels of several circRNAs in OSCC clinical samples, in which circCPNE1 (hsa_circ_0001146) from the CPNE1 gene on chromosome 20 was under-expressed in OSCC compared with para-cancerous tissues (Supporting Information Figs. S1A and S1B). Here, we examined the expression levels of circCPNE1 in 33 pairs of OSCC

tissues and para-cancerous tissues by qRT-PCR and found that the expression of circCPNE1 was lower in OSCC tissues than in para-cancerous tissues (Fig. 1A and Fig. S1C). Moreover, the expression level of circCPNE1 showed a significantly negative correlation with the clinical stage of OSCC patients (Fig. 1B and Supporting Information Table S3). Consistently, FISH staining showed lower expression of circCPNE1 in OSCC tissues compared with para-cancerous tissues (Fig. 1C and D, and Fig. S1D). At the cellular level, the expression level of circCPNE1 in OSCC cell lines (Cal27, HSC2, and Cal33) was significantly lower than that in NOK (Fig. 1E). The Cal27 and HSC2 cell lines were selected for subsequent experiments because their circCPNE1 expression levels were comparable and lower than Cal33. RNase R was used to verify the stability of circRNA because it can rapidly digest all linear RNAs but cannot easily digest circRNA (Fig. 1F). Extracted total RNA was treated with

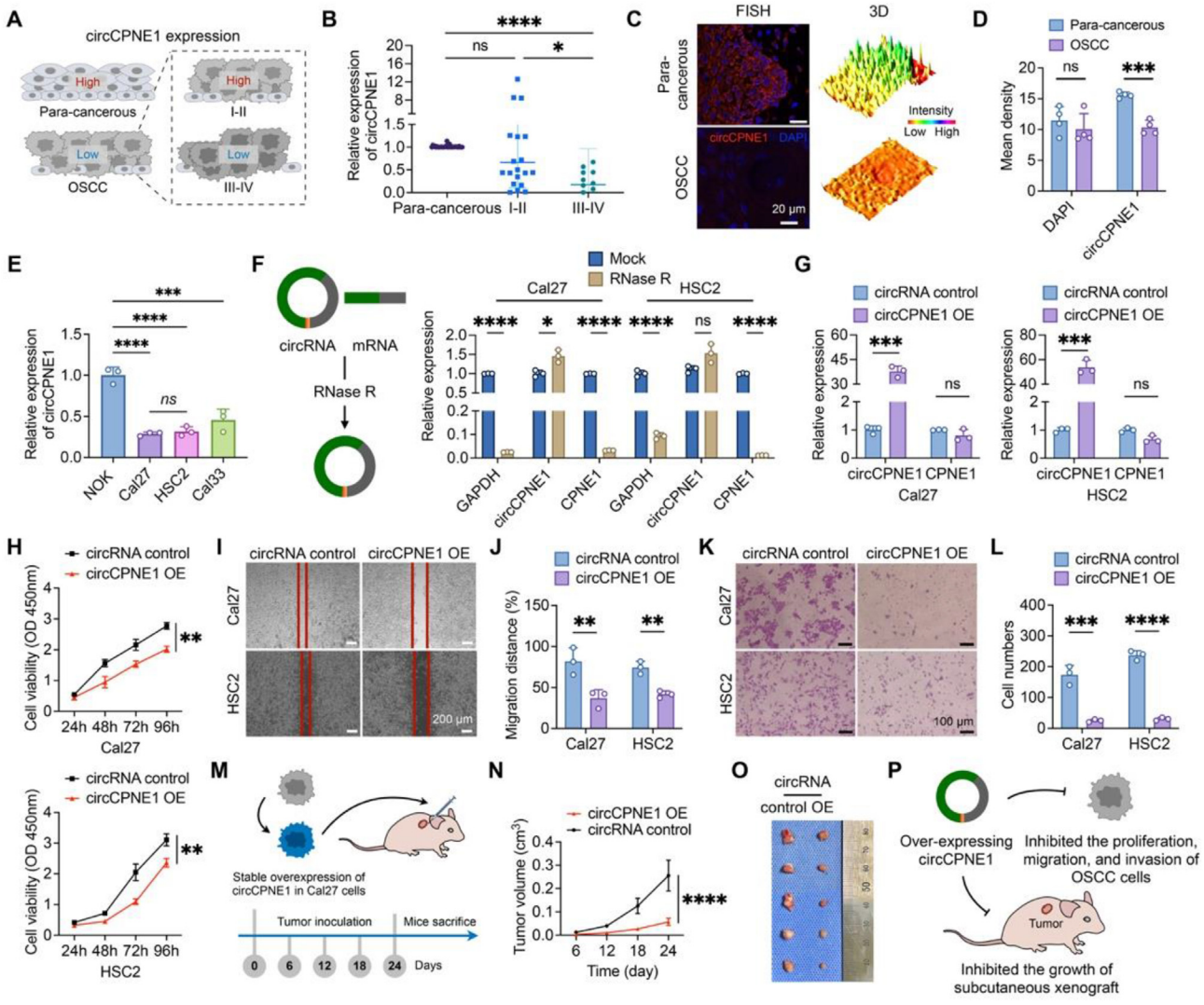

Figure 1 Identification and function of circCPNE1 in OSCC. (A) Schematic of circCPNE1 expression in OSCC tissues demonstrating high expression of circCPNE1 in para-cancerous tissues (compared with OSCC tissues) and clinical stages I−II (compared with stages III−IV), respectively. (B) circCPNE1 expression was determined by qRT-PCR in para-cancerous tissues and OSCC tissues in clinical stages I−II and III−IV ($n = 33$). FISH staining assay, 3D reconstruction (C) and fluorescence quantitative analysis (D) showed that the expression of circCPNE1 was lower in OSCC tissues than in para-cancerous tissues ($n = 4$). (E) The expression of circCPNE1 in the NOK, Cal27, HSC2, and Cal33 cell lines was examined by qRT-PCR assay. (F) circRNA was resistant to RNase R treatment. qRT-PCR analysis of circCPNE1 and *CPNE1* expression in OSCC cells treated with RNase R. *GAPDH* was used as a negative control. (G) Expression levels of circCPNE1 and *CPNE1* were assessed by qRT-PCR after overexpression of circCPNE1 in OSCC cells. (H) CCK-8 assays were performed to examine the effect of overexpressing circCPNE1 on the proliferation of OSCC cells. (I, J) Wound healing assays of indicated OSCC cells at 24 h. Scale bar = 200 μm. (K, L) Transwell invasion assays of indicated OSCC cells. Scale bar = 100 μm. (M) Experimental timeline of Cal27 cells transfected with lentivirus to stably overexpress circCPNE1 and Cal27 control cells, which were subcutaneously transplanted in nude mice. (N) Tumor volume growth curves of tumor-bearing mice. (O) Representative gross view of tumors from nude mice on Day 24. (P) Schematic of the effects of circCPNE1 overexpression on OSCC *in vivo* and *in vitro*. Data are presented as mean ± SD of more than three independent experiments. *$P < 0.05$, **$P < 0.01$, ***$P < 0.001$, ****$P < 0.0001$ *versus* controls. OE, overexpression.

RNase R, and qRT-PCR results revealed that circCPNE1 was more resistant to RNase R than the linear gene *CPNE1* and *GAPDH* (Fig. 1F).

Because the expression level of circCPNE1 was low in OSCC cells, we characterized the function of circCPNE1 with a circCPNE1-specific overexpression plasmid, which effectively overexpressed circCPNE1 without any effect on *CPNE1* (Fig. 1G). Gain-of-function assays demonstrated that circCPNE1 significantly inhibited the proliferation (Fig. 1H), migration (Fig. 1I and J, and Supporting Information Fig. S2), and invasion (Fig. 1K and L) abilities of OSCC cells. We then constructed a Cal27 cell line stably overexpressing circCPNE1 (Supporting Information Fig. S3A−S3C) and assessed the effect of circCPNE1 on tumor growth *in vivo* through a subcutaneous transplantation model in nude mice (Fig. 1M). The results showed that the tumor volume growth rate and size in the circCPNE1 overexpression (OE) group were slower and smaller than the control group, respectively (Fig. 1N and O). Altogether, our data suggest that circCPNE1 is downregulated in OSCC tissues, correlates with clinical stages, and could inhibit the malignant progression of OSCC cells (Fig. 1P).

3.2. *CircCPNE1 as a sponge for miR-330-3p and the effect of miR-330-3p on OSCC cells*

The function of circRNAs is closely related to their cellular localization, and circRNAs localized at the cytoplasm are recognized to act as miRNA sponges[1]. In the present study, FISH staining revealed that circCPNE1 was localized in the cytoplasm, with a similar localization to the cytoplasmic marker 18SRNA (Fig. 2A and Supporting Information Fig. S4A). Nucleocytoplasmic segregation experiments also revealed that circCPNE1 was mainly expressed in the cytoplasm (Fig. 2B). Collectively, these results suggest that circCPNE1 may act as a miRNA sponge. The AGO2 protein is used as an indicator that circRNAs act as a miRNA sponge. The CircInteractome database reports that circCPNE1 has 23 potential binding sites to AGO2 (Fig. S4B). This was then verified by RIP-PCR assays, which showed that the anti-AGO2 antibody successfully decreased circCPNE1 levels compared with the control IgG (Fig. 2C and D).

Furthermore, four databases (CircInteractome, ENCORI, circBank, and TargetScan) were used to predict miRNAs that might bind to circCPNE1, and the results suggested miR-330-3p and miR-520h as the most potential downstream targets (Fig. 2E). Next, we investigated whether miR-330-3p and miR-520h could act as downstream targets of circCPNE1 and influence the development of OSCC. First, decreased expression levels of both miR-330-3p and miR-520h were observed in the circCPNE1 OE group, suggesting that circCPNE1 overexpression might inhibit the expression of miR-330-3p and miR-520h (Fig. 2F). Therefore, we overexpressed miR-330-3p and miR-520h to examine their functions; by transfection with the corresponding mimics, we successfully increased the expression levels of miR-330-3p and miR-520h in OSCC cells (Fig. 2G and Supporting Information Fig. S5A). The results of gain-of-function experiments showed that miR-330-3p overexpression was associated with a significant enhancement of proliferation, migration, and invasion of OSCC cells (Fig. 2H−L), whereas miR-520h overexpression had no significant effect on OSCC cells (Fig. S5B−S5F). Therefore, we hypothesized that miR-330-3p might be a key gene affecting OSCC progression and performed a dual luciferase reporter assay. We constructed a wild-type (WT) circCPNE1 with linear sequences and a mutant-type (MT) circCPNE1 with a mutated miR-330-3p binding site and cloned them into a luciferase reporter vector, which was then transfected into OSCC cells. The transfection of these OSCC cells with miR-330-3p mimics showed that the luciferase activity was significantly reduced after co-transfection of miR-330-3p mimics and WT circCPNE1, whereas no significant changes were observed in the MT circCPNE1 group. These findings indicate that miR-330-3p binds to circCPNE1 (Fig. 2M). FISH staining also revealed that circCPNE1 and miR-330-3p had similar cellular sub-localization, further demonstrating that miR-330-3p binds to circCPNE1 (Fig. 2N). The above results suggest that miR-330-3p may act as a key downstream target of circCPNE1 that affects the progression of OSCC cells (Fig. 2O).

3.3. *The circCPNE1/miR-330-3p pathway is involved in regulating OSCC processes and affects the expression of SOX6*

Rescue experiments were performed to investigate the effect of the interaction between circCPNE1 and miR-330-3p, and the results showed that miR-330-3p overexpression reversed the inhibition of OSCC proliferation (Fig. 3A), migration (Fig. 3B and C, and Supporting Information Fig. S6), and invasion (Fig. 3D and E) by circCPNE1 overexpression, further demonstrating the role of the circCPNE1/miR-330-3p axis in regulating OSCC progression (Fig. 3F).

We then screened 97 genes by analyzing five databases (miRDB, miRWalk, microT, miRmap, and TargetScan) to predict potential binding targets for miR-330-3p (Supporting Information Fig. S7A). According to numerous published studies, circRNA and mRNA in the circRNA/miRNA/mRNA signaling pathway have similar expression patterns and the same regulatory roles in specific disease models. To screen for the optimal candidate mRNAs, we analyzed the Gene Expression Omnibus (GEO) database (GSE36090 and GSE37991), which revealed dysregulated genes in OSCC *versus* para-cancerous tissues (Fig. S7B). We then intersected the genes that were significantly downregulated in the GSE36090 and GSE37991 databases with 97 potential target mRNAs to obtain *ADD3*, *AMOT*, *EBF1*, *ERBB4*, *SOX6*, and *USP15* (Fig. 3G). Published literature revealed that *ADD3*[26], *AMOT*[27], *EBF1*[28], and *USP15*[29] primarily acted as protumor factors, whereas *ERBB4*[30] and *SOX6*[31,32] mainly functioned as tumor suppressors in various tumors. Therefore, we chose *ERBB4* and *SOX6* as the next targets of our study. The qRT-PCR assay revealed that the mRNA expression levels of *ERBB4* and *SOX6* were positively regulated by circCPNE1 and negatively regulated by miR-330-3p (Fig. 3H). Western blotting experiments revealed that the protein expression level of ERBB4 was barely affected by the regulation of circCPNE1 and miR-330-3p, whereas the protein expression level of SOX6 was regulated by both circCPNE1 and miR-330-3p (Fig. 3I). Therefore, *SOX6* most likely acts as a downstream target of the circCPNE1/miR-330-3p axis. Consistent with the results of the *in vitro* experiments, the AKT and Bcl-2 protein levels were negatively regulated by circCPNE1 and positively regulated by miR-330-3p (Fig. 3I). Furthermore, we verified that miR-330-3p could bind to *SOX6* with a dual luciferase reporter assay (Fig. 3J). In addition, we found that SOX6 expression was significantly higher in the circCPNE1 OE group than the control group in the subcutaneous tumors of nude mice (Fig. 3K and L, and Supporting Information Fig. S8), which further indicates that *SOX6* is a downstream target of the circCPNE1/miR-330-3p axis. In conclusion, we found that the circCPNE1/miR-

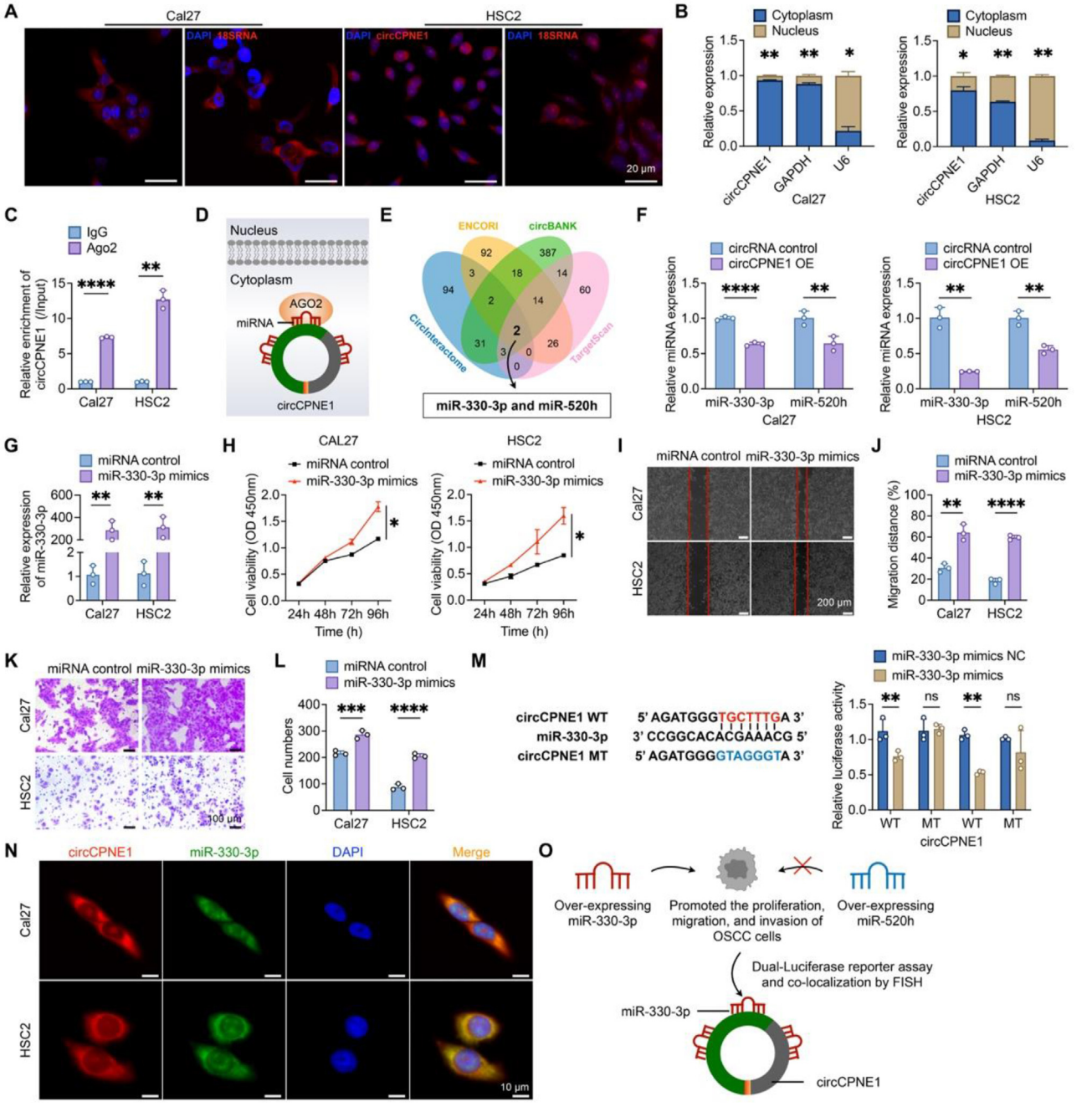

Figure 2 circCPNE1 as a miR-330-3p sponge. (A) FISH was performed to observe the cellular location of circCPNE1 in cells; 18S RNA was used as a positive control for cytoplasmic localization. Scale bar = 20 μm. (B) OSCC cells were subcellularly fractionated and then analyzed for circCPNE1 expression by RT-qPCR. *GAPDH* and *U6* were used as controls for the cytoplasmic and nuclear fractions, respectively. (C) RIP assay using control IgG or anti-AGO2 antibody on OSCC cells followed by qRT-PCR to detect enrichment of circCPNE1. (D) Schematic diagram of the binding of circCPNE1 to AGO2 localized in the cytoplasm. (E) Venn diagram of miRNAs that could be regulated by circCPNE1. (F) Expression levels of miR-330-3p and miR-520h were assessed by qRT-PCR after overexpression of circCPNE1 in OSCC cells. (G) The expression level of miR-330-3p was assessed by qRT-PCR after transfection with miR-330-3p mimics in OSCC cells. (H) CCK-8 assays were performed to examine the effect of miR-330-3p overexpression on the proliferation of OSCC cells. (I, J) Wound healing assays of indicated OSCC cells at 24 h. Scale bar = 200 μm. (K, L) Transwell invasion assays of indicated OSCC cells. Scale bar = 100 μm. (M) Schematic diagram showing the sequence alignment of miR-330-3p with circCPNE1. A dual luciferase reporter assay was performed on miR-330-3p and circCPNE1. (N) FISH was performed to observe the cellular location of circCPNE1 (red) and miR-330-3p (green) in cells. Scale bar = 10 μm. (O) Schematic of the function of circCPNE1 as a miR-330-3p sponge and the effect of miR-330-3p on OSCC. Data are presented as mean ± SD of more than three independent experiments. $^{*}P < 0.05$, $^{**}P < 0.01$, $^{***}P < 0.001$, $^{****}P < 0.0001$ *versus* controls. OE, overexpression; WT, wild-type; MT mutant-type.

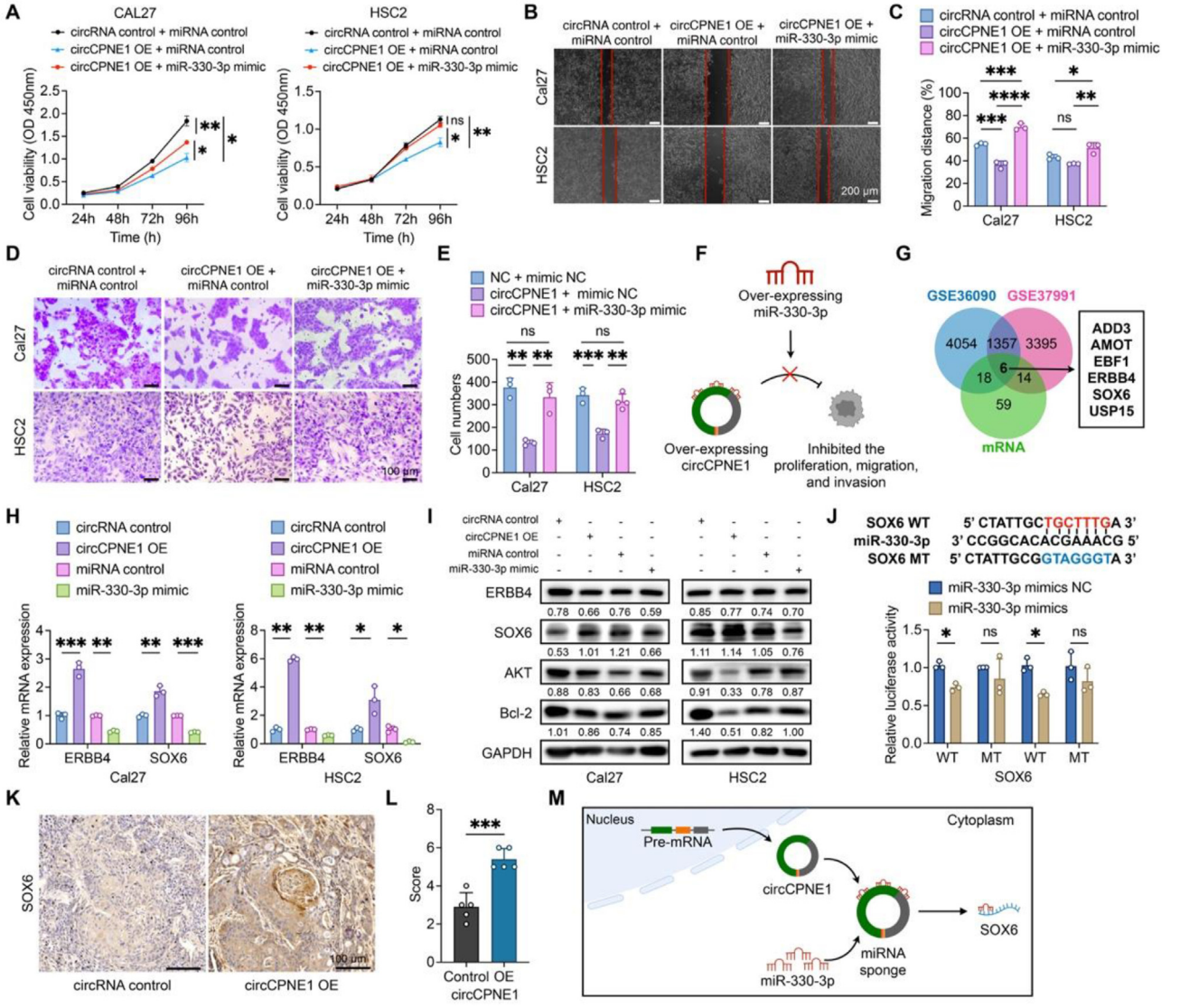

Figure 3 circCPNE1/miR-330-3p/*SOX6* pathway in OSCC. (A) CCK-8 assays were performed to examine the effect of circCPNE1 and miR-330-3p overexpression on OSCC cell proliferation. (B, C) Wound healing assays of indicated OSCC cells at 24 h. Scale bar = 200 μm. (D, E) Transwell invasion assays of indicated OSCC cells. Scale bar = 100 μm. (F) Schematic illustration of the ability of miR-330-3p overexpression to rescue the inhibitory effects of circCPNE1 overexpression on OSCC cells. (G) Venn diagram of mRNAs that could be regulated by miR-330-3p. (H) Expression levels of *ERBB4* and *SOX6* were assessed by qRT-PCR of indicated OSCC cells. (I) Western blot assays were performed to detect the expression of ERBB4, SOX6, AKT, Bcl-2, and GAPDH in indicated OSCC cells. (J) Schematic diagram showing the sequence alignment of miR-330-3p with *SOX6*. A dual luciferase reporter assay was performed on miR-330-3p and *SOX6*. (K, L) IHC staining and quantitative scoring were used to analyze the SOX6 protein levels. Scale bar = 100 μm. (M) Schematic illustration of the circCPNE1/miR-330-3p/*SOX6* pathway in OSCC. Data are presented as mean ± SD of more than three independent experiments. $^{*}P < 0.05$, $^{**}P < 0.01$, $^{***}P < 0.001$, $^{****}P < 0.0001$ *versus* controls. OE, overexpression; WT, wild-type; MT mutant-type.

330-3p/*SOX6* signaling pathway may be involved in regulating OSCC development (Fig. 3M).

3.4. *Preparation and characterization of PP@miR NPs*

We prepared a reduction-responsive cisplatin prodrug polymer (Pt [IV]−PLys, PP) by the hydrophilic modification of cisplatin with polylysine (Fig. 4A). The chemical structure of PP was characterized by infrared spectroscopy (Supporting Information Fig. S9A), and 3512 and 554 cm^{-1} were identified as the stretching vibration peaks of −OH on Pt−OH [IV]. The obtained Pt−OH was modified with polylysine *via* maleic anhydride, and the characteristic peaks at 3512 and 554 cm^{-1} disappeared in the product, which in turn appeared as the characteristic peaks of amide bonds on polylysine at 1543 and 1640 cm^{-1}. In ^{1}H NMR spectra (Fig. S9B), compared with polylysine, new hydrogen atomic absorption peaks appeared in the spectrum of PP at 2.25−2.5 ppm, which belonged to the hydrogen atom on methylene group on maleic anhydride, indicating that PP was prepared successfully. The MALDI−TOF result showed that PP had two relatively broad peaks at 4593 and 8946, indicating that the maximum molecular weight of PP was about 8946 (Fig. S9C). In

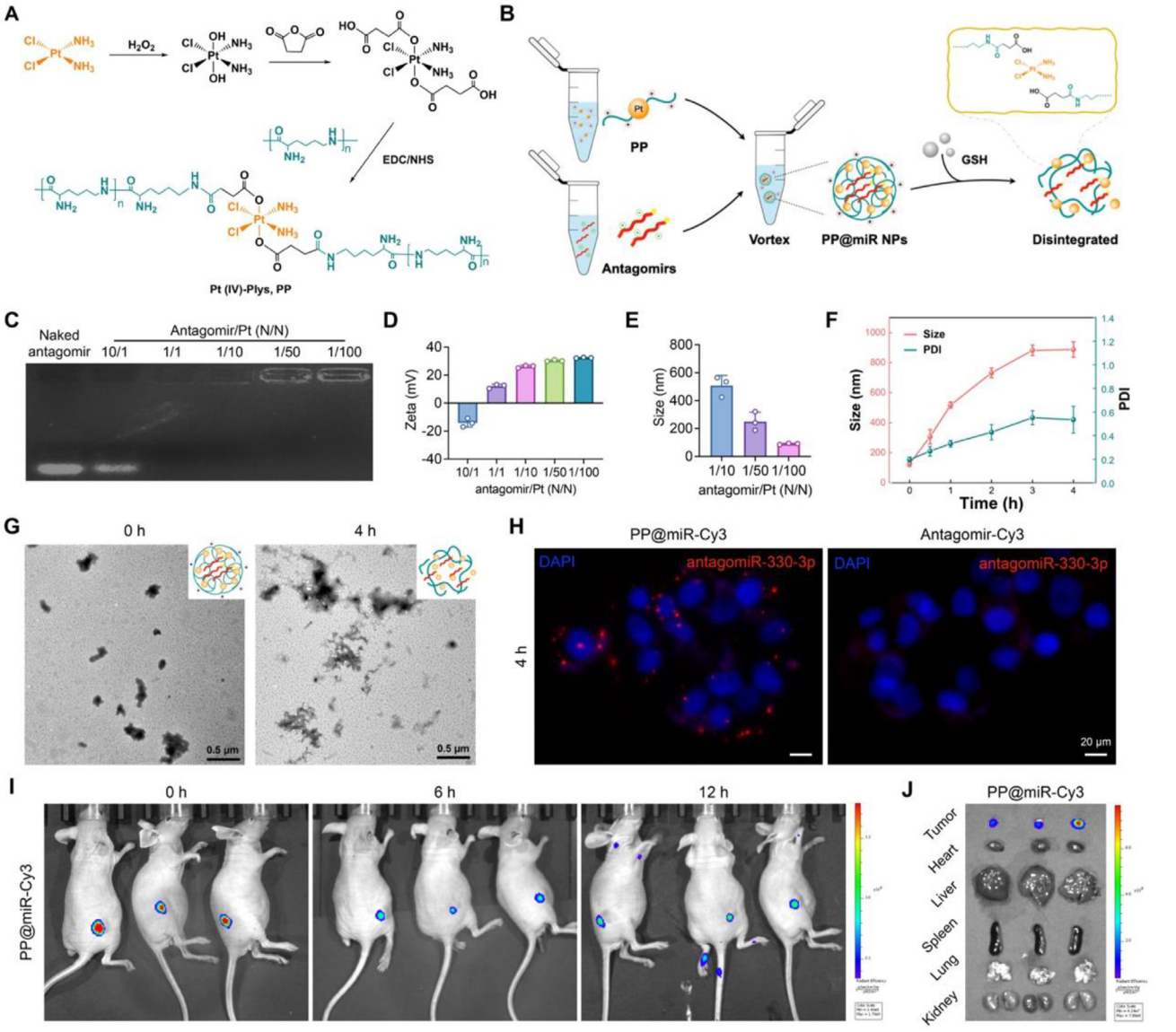

Figure 4 Preparation and characterization of PP@miR NPs. (A) Schematic of the synthetic route of cisplatin prodrugs. (B) Schematic of the preparation of PP@miR NPs. (C) Gel electrophoresis shows the loading of RNA at different ratios of cisplatin prodrug to antagomirs. (D, E) DLS detection of zeta potential and particle size of NPs with different ratios of cisplatin prodrug to RNA. (F) Detection of size and PDI changes of NPs by DLS under GSH. (G) Morphology of NPs at different time points detected by TEM under GSH. Scale bar = 0.5 μm. (H) Cellular uptake of PP@miR-Cy3 NPs and antagomir-Cy3 by Cal27 cells at 4 h. Scale bar = 20 μm. Fluorescence images of tumor sites (I) at 0, 6, and 12 h and fluorescence images of heart, liver, spleen, lungs, and kidneys (J) at 12 h in tumor-bearing nude mice after paratumoral injection of PP@miR-Cy3 NPs. Data are presented as mean ± SD of more than three independent experiments.

addition, after freeze-drying, PP was weighed, and the content of platinum was about 3.97% (*w*/*w*). Polylysine contains many amino groups that cause PP to be positively charged and allow its assembly into reduction-responsive NPs (PP@miR NPs) by electrostatic interactions with negatively charged antagomirs (Fig. 4B). The results of gel electrophoresis showed that when the molar ratio of antagomirs to Pt was greater than 1:1, antagomirs were completely encapsulated by PP@miR NPs (Fig. 4C). In addition, the zeta potential of PP@miR NPs increased and the particle size decreased with an increase in Pt (Fig. 4D and E). Under the action of GSH, the particle size of the PP@miR NPs gradually increased, and the PDI value increased, indicating that PP@miR NPs were gradually disintegrated under GSH (Fig. 4F). While in PBS, the PP@miR NPs were stable for the first 4 h at 37 °C but tended to aggregate into larger particles in the later time, and it could be stable for at least 72 h at 4 °C (Supporting Information Fig. S10). TEM also showed that the NPs gradually depolymerized in response to GSH (Fig. 4G). Antagomirs were released about 27% in the presence of 10 mmol/L GSH whereas less was released in PBS after 6 h (Supporting Information Fig. S11). Cellular uptake assays showed that Cal27 cells demonstrated significant uptake of PP@miR-Cy3 but no uptake of antagomir-Cy3 after adding them to the culture medium for 4 h (Fig. 4H and Supporting Information Fig. S12). *In vivo* biodistribution experiments, PP@miR-Cy3 was mainly distributed around the tumor after para-tumor injection of NPs in nude mice,

and the fluorescence was weakened due to the aggregation effect (Fig. 4I). Whereas the antithrombin-Cy3 group exhibited strong fluorescence that was scattered on the skin surface of nude mice (Supporting Information Fig. S13A). Nude mice were dissected after 12 h, and it could be seen that the drug mainly accumulated around the tumor and was not distributed in major organs (Fig. 4J and Fig. S13B).

3.5. *PP@miR NPs inhibited OSCC progression and partially eliminated tumors*

Subcutaneous xenograft tumor models were established in nude mice and divided into five groups (PBS, antagomir, PP, PP@miR-NC NPs, and PP@miR NPs) according to the administration of the drugs, which were injected around the tumor every other day (Fig. 5A). The experimental results showed that the PP@miR NPs group achieved the most significant tumor suppression, successfully resulting in the complete regression of 2 out of 5 tumors (Fig. 5B) and the smallest tumor volume and mass among all groups (Fig. 5C and D); all groups showed good biosafety (Supporting Information Fig. S14). The results of TUNEL staining showed that the PP@miR group had the most significant pro-apoptotic effect on tumor cells (Fig. 5E and Supporting Information Fig. S15). IHC revealed that the PP@miR group exhibited the strongest inhibition of tumor cell proliferation (Fig. 5F and G), the greatest expression of SOX6 protein (Fig. 5F and H), and the strongest inhibition of tumor blood vessel formation (Fig. 5F).

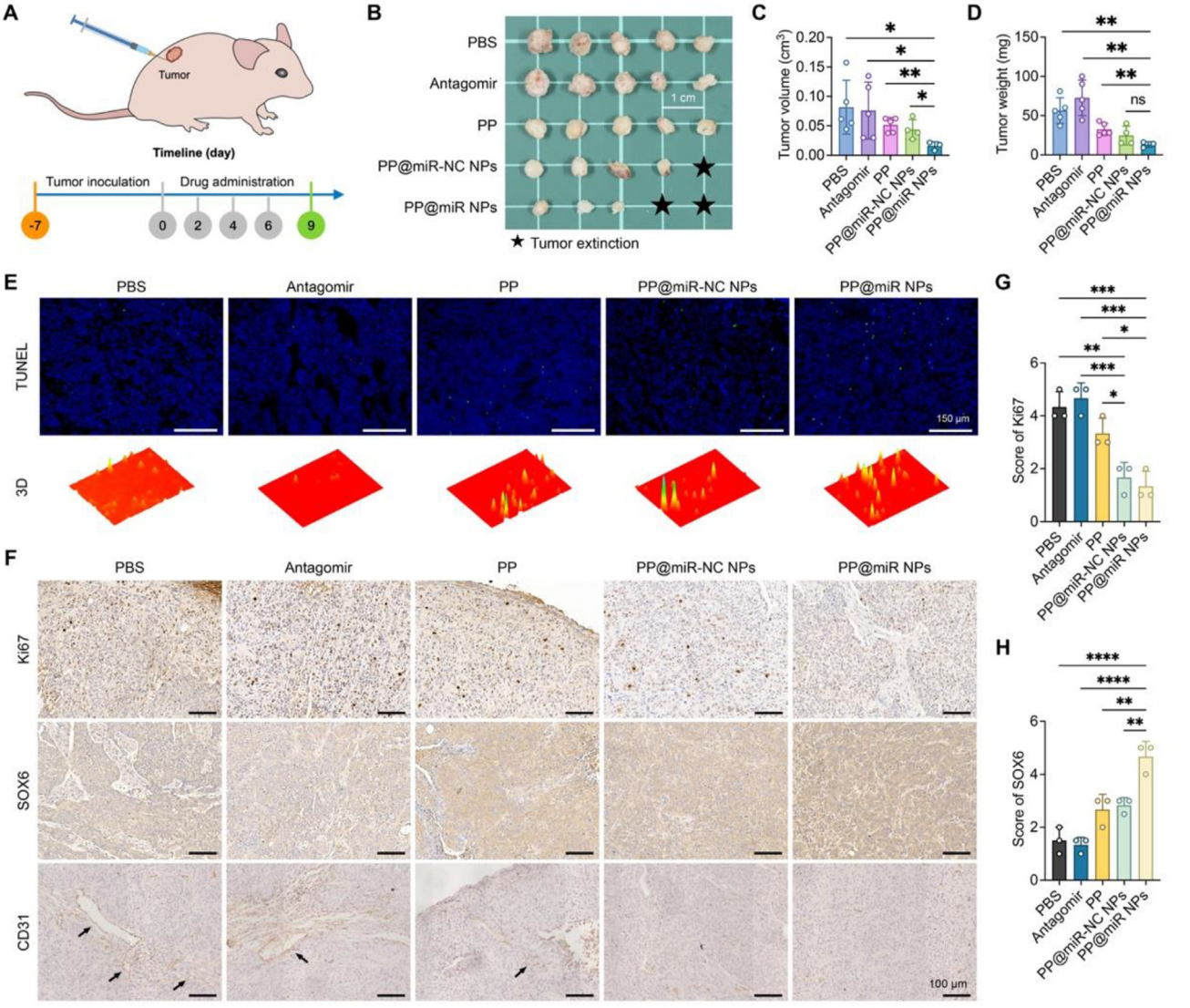

Figure 5 The effects of PP@miR NPs on OSCC *in vivo*. (A) Schematic of the treatment route for nude mice. (B) Photographs of tumors in nude mice after treatments ($n = 5$). Scale bar = 1 cm. Tumor volume (C) and weight (D) of nude mice ($n = 5$). (E) TUNEL staining results and 3D reconstruction. Scale bar = 150 μm. (F) IHC staining results of Ki67, SOX6, and CD31. Arrows indicated microvessels. Scale bar = 100 μm. Quantitative scoring results of Ki67 (G) and SOX6 (H). Data are presented as mean ± SD. $^{*}P < 0.05$, $^{**}P < 0.01$, $^{***}P < 0.001$, $^{****}P < 0.0001$ *versus* controls. NPs, nanoparticles; NC, negative control.

4. Discussion

As classical ncRNAs, circRNA and miRNA are known to be involved in the malignant processes of various tumors and are associated with resistance to cancer therapies[33]. Conventional treatments for OSCC, such as surgery and radiotherapy, are not satisfactory because they are often associated with severe systemic adverse effects. However, miRNA-based gene therapy, a novel targeted therapeutic approach, has achieved promising results in experimental tumor management[34], and the selective elimination of relevant oncogenic miRNAs may become a new strategy for OSCC treatment.

In this study, we identified a circRNA/miRNA axis that regulates the OSCC process, and we prepared a drug delivery system targeting the specific miRNA with NPs. A meta-analysis identified circRNAs as promising biomarkers and therapeutic targets for OSCC[35]. Here, we identified and validated circCPNE1, a circRNA localized at the cytoplasm of OSCC cells with tumor suppressive effects, whose function has rarely been reported. The expression level of circCPNE1 was significantly lower in OSCC tissues and cells compared with para-cancerous tissues and normal oral keratinocytes. Moreover, the expression level of circCPNE1 was significantly negatively correlated with the clinical stage of patients with OSCC, suggesting that it could be used as a biomarker to indicate a patient's clinical stage. We then validated the tumor suppressive ability of circCPNE1, which inhibited the proliferation, migration, and invasion of OSCC cells *in vitro* as well as the growth of subcutaneous xenografts *in vivo*. Furthermore, we identified miR-330-3p, a key downstream target of circCPNE1, by combining bioinformatics database analysis with RIP-PCR, FISH, and dual luciferase reporter experiments.

Many recent studies have identified miR-330-3p as a tumor promoter. For instance, miR-330-3p can promote the proliferation, migration, and metastasis of breast cancer cells[36,37]. In addition, miR-330-3p is identified as a potential key downstream target of circRBPMS, promoting the proliferation, migration, invasion, and EMT pathway of bladder cancer cells[38]. Moreover, miR-330-3p can act as the downstream target of several circRNAs to affect the progression of prostate cancer[39], colon cancer[40], and osteosarcoma[41], but it is rarely reported in OSCC. According to the GEO database (GSE137865 and GSE28100) results, the expression of miR-330-3p in OSCC was higher than that in normal tissues adjacent to cancer tissue (Supporting Information Fig. S16). Our experimental results showed that miR-330-3p had obvious protumor abilities, promoting the proliferation, migration, and invasion of OSCC cells, and we found that miR-330-3p could reverse the inhibitory effect of circCPNE1 on OSCC cells. We also found that miR-330-3p could inhibit the mRNA and protein expression levels of SOX6 through qRT-PCR, Western blotting, and IHC experiments. Multiple studies have reported that *SOX6* acts as a typical tumor suppressor in various cancers, such as esophageal squamous carcinoma[42], pancreatic cancer[43], and prostate cancer[44]. Therefore, the inhibition of miR-330-3p may serve as a key target for suppressing OSCC progression.

After obtaining the above results, we selectively inhibited the expression of miR-330-3p in OSCC cells. RNA possesses a large amount of negative charge and can bind to positively charged substances through electrostatic interactions, allowing them to be loaded into NPs to extend the RNA half-life *in vivo* and target its delivery to tumor cells[45]. Studies have shown that cisplatin inhibited the growth of OCSS, but cisplatin resistance remains an important issue[46]. On this basis, we prepared a cisplatin prodrug polymer with a polylysine fraction enriched with a large number of amino groups, which could effectively bind RNA. Cisplatin was assembled with antagomirs by simple vortex to form reduction-responsive PP@miR NPs that gradually dispersed in response to high concentrations of GSH inside tumor cells. The common practice is to encapsulate platinum-based drugs in liposomes to increase their bioavailability and reduce toxicity[47]. Here, we loaded and released miRNA inhibitors using a modified cisplatin prodrug as a carrier. This nanomaterial may not be as stable as liposomes, but it has a simplified preparation process and material composition, which facilitates mechanism studies and, which in turn improves our nanomedicines. The enhanced permeability and retention (EPR) effect on tumors is controversial, and although nanoparticles have shown great advantages over free drugs in preclinical studies, only a small fraction of all drugs are aggregated at tumor sites[48,49]. Compared with systemic drug delivery, paratumoral administration allows better drug enrichment at the tumor site, especially for superficial tumors, such as OSCC. Paratumoral injection of PP NPs showed significant therapeutic effects; PP@miR NPs exhibited better tumor suppression in comparison with PP@miR-NC NPs and even achieved partial tumor regression.

5. Conclusions

In this study, we determined that the circCPNE1 level was associated with the clinical stage of OSCC; we then validated the ability of the circCPNE1/miR-330-3p pathway to suppress OSCC tumors and regulate the expression levels of the SOX6, AKT, and Bcl-2 proteins. Because miR-330-3p played an important role as a tumor-promoting factor, we developed an antagomir delivery system (PP@miR NPs) to target this microRNA. Our delivery system based on a cationic cisplatin prodrug effectively inhibited OSCC progression and even achieved partial tumor regression. Overall, we used circCPNE1 to screen for miR-330-3p, a key target regulating the OSCC process, and confirmed that its associated antagomir delivery system was effective in treating OSCC. These findings provide new insights into potential OSCC therapies.

Acknowledgments

This work was supported by National Natural Science Foundation of China grants (Nos. 82073000, 51973136, 81902779, and 82173326), Science Foundation of Sichuan Province (No. 2022YFS0289, China). Interdisciplinary innovation project of West China College of Stomatology, Sichuan University (RD-03-202004, China).

Author contributions

Xinhua Liang, Yaling Tang, and Yong Sun designed the research. Huayang Fan and Mingda Zhao carried out the experiments and performed data analysis. Hongjie Jiang and Zhenwei Yu participated in part of the experiments. Huayang Fan and Mingda Zhao drafted the manuscript. Xinhua Liang, Yaling Tang, Yujiang Fan, and Yong Sun revised the manuscript. All of the authors have read and approved the final manuscript.

Conflicts of interest

The authors have no conflicts of interest to declare.

Appendix A. Supporting information

Supporting data to this article can be found online at https://doi.org/10.1016/j.apsb.2024.02.009.

References

1. Kristensen LS, Jakobsen T, Hager H, Kjems J. The emerging roles of circRNAs in cancer and oncology. *Nat Rev Clin Oncol* 2022;**19**:188−206.
2. Fan HY, Jiang J, Tang YJ, Liang XH, Tang YL. CircRNAs: a new chapter in oral squamous cell carcinoma biology. *OncoTargets Ther* 2020;**13**:9071−83.
3. Zhang Q, Wang W, Zhou Q, Chen C, Yuan W, Liu J, et al. Roles of circRNAs in the tumour microenvironment. *Mol Cancer* 2020;**19**:14.
4. Liu J, Jiang X, Zou A, Mai Z, Huang Z, Sun L, et al. circIGHG-induced Epithelial-to-Mesenchymal transition promotes oral squamous cell carcinoma progression *via* miR-142-5p/IGF2BP3 signaling. *Cancer Res* 2021;**81**:344−55.
5. Saikishore R, Velmurugan P, Ranjithkumar D, Latha R, Sathiamoorthi T, Arun A, et al. The circular RNA-miRNA axis: a special RNA signature regulatory transcriptome as a potential biomarker for OSCC. *Mol Ther Nucleic Acids* 2020;**22**:352−61.
6. Zhang X, Hai L, Gao Y, Yu G, Sun Y. Lipid nanomaterials-based RNA therapy and cancer treatment. *Acta Pharm Sin B* 2023;**13**:903−15.
7. Meng X, Lou QY, Yang WY, Wang YR, Chen R, Wang L, et al. The role of non-coding RNAs in drug resistance of oral squamous cell carcinoma and therapeutic potential. *Cancer Commun* 2021;**41**:981−1006.
8. Foss FM, Querfeld C, Kim YH, Pinter-Brown LC, William BM, Porcu P, et al. Ph 1 study of MRG-106, an inhibitor of miR-155, in CTCL. *J Clin Oncol* 2018;**36**:2511.
9. Janssen HL, Reesink HW, Lawitz EJ, Zeuzem S, Rodriguez-Torres M, Patel K, et al. Treatment of HCV infection by targeting microRNA. *N Engl J Med* 2013;**368**:1685−94.
10. Krützfeldt J, Rajewsky N, Braich R, Rajeev KG, Tuschl T, Manoharan M, et al. Silencing of microRNAs *in vivo* with 'antagomirs'. *Nature* 2005;**438**:685−9.
11. Han S, Xue L, Wei Y, Yong T, Jia W, Qi Y, et al. Bone lesion-derived extracellular vesicles fuel prometastatic cascades in hepatocellular carcinoma by transferring ALKBH5-targeting miR-3190-5p. *Adv Sci* 2023;**10**:e2207080.
12. Lo YL, Lin HC, Tseng WH. Tumor pH-functionalized and charge-tunable nanoparticles for the nucleus/cytoplasm-directed delivery of oxaliplatin and miRNA in the treatment of head and neck cancer. *Acta Biomater* 2022;**153**:465−80.
13. Yi W, Tu MJ, Liu Z, Zhang C, Batra N, Yu AX, et al. Bioengineered miR-328-3p modulates GLUT1-mediated glucose uptake and metabolism to exert synergistic antiproliferative effects with chemotherapeutics. *Acta Pharm Sin B* 2020;**10**:159−70.
14. Johnson DE, Burtness B, Leemans CR, Lui VWY, Bauman JE, Grandis JR. Head and neck squamous cell carcinoma. *Nat Rev Dis Prim* 2020;**6**:92.
15. Rottenberg S, Disler C, Perego P. The rediscovery of platinum-based cancer therapy. *Nat Rev Cancer* 2021;**21**:37−50.
16. Ferreira JA, Peixoto A, Neves M, Gaiteiro C, Reis CA, Assaraf YG, et al. Mechanisms of cisplatin resistance and targeting of cancer stem cells: adding glycosylation to the equation. *Drug Resist Updates* 2016;**24**:34−54.
17. Boztepe T, Castro GR, León IE. Lipid, polymeric, inorganic-based drug delivery applications for platinum-based anticancer drugs. *Int J Pharm* 2021;**605**:120788.
18. Goldberg M, Manzi A, Birdi A, Laporte B, Conway P, Cantin S, et al. A nanoengineered topical transmucosal cisplatin delivery system induces anti-tumor response in animal models and patients with oral cancer. *Nat Commun* 2022;**13**:4829.
19. Agrawal N, Izumchenko E, Hodge K, Young S, Melville JC, Shum J, et al. A phase II study of PRV111 nanoengineered cisplatin patch as a neoadjuvant therapy for early-stage oral squamous cell carcinoma (OSCC). *J Clin Oncol* 2021;**39**:6056.
20. Meng X, Ma F, Yu D. The diverse effects of cisplatin on tumor microenvironment: insights and challenges for the delivery of cisplatin by nanoparticles. *Environ Res* 2024;**240**:117362.
21. Garcia-Peiro JI, Bonet-Aleta J, Santamaria J, Hueso JL. Platinum nanoplatforms: classic catalysts claiming a prominent role in cancer therapy. *Chem Soc Rev* 2022;**51**:7662−81.
22. Zhang L, Ye B, Chen Z, Chen ZS. Progress in the studies on the molecular mechanisms associated with multidrug resistance in cancers. *Acta Pharm Sin B* 2023;**13**:982−97.
23. Yan J, Zhang Y, Zheng L, Wu Y, Wang T, Jiang T, et al. Let-7i miRNA and platinum loaded nano-graphene oxide platform for detection/reversion of drug resistance and synergetic chemical−photothermal inhibition of cancer cell. *Chin Chem Lett* 2022;**33**:767−72.
24. Jafarzadeh A, Paknahad MH, Nemati M, Jafarzadeh S, Mahjoubin-Tehran M, Rajabi A, et al. Dysregulated expression and functions of microRNA-330 in cancers: a potential therapeutic target. *Biomed Pharmacother* 2022;**146**:112600.
25. Wang S, Pang X, Tong L, Fan H, Jiang J, Zhao M, et al. LncRNA SELL/L-selectin promotes HPV-positive HNSCC progression and drives fucoidan-mediated therapeutic strategies. *Acta Biomater* 2023;**167**:436−48.
26. Rani SB, Rathod SS, Karthik S, Kaur N, Muzumdar D, Shiras AS. MiR-145 functions as a tumor-suppressive RNA by targeting Sox9 and adducin 3 in human glioma cells. *Neuro Oncol* 2013;**15**:1302−16.
27. Lin X, Spindler TJ, de Souza Fonseca MA, Corona RI, Seo JH, Dezem FS, et al. Super-enhancer-associated LncRNA UCA1 interacts directly with AMOT to activate YAP target genes in epithelial ovarian cancer. *iScience* 2019;**17**:242−55.
28. Liu GM, Lu TC, Sun ML, Ji X, Zhao YA, Jia WY, et al. RP11-874J12.4 promotes oral squamous cell carcinoma tumorigenesis *via* the miR-19a-5p/EBF1 axis. *J Oral Pathol Med* 2020;**49**:645−54.
29. Zou Q, Jin J, Hu H, Li HS, Romano S, Xiao Y, et al. USP15 stabilizes MDM2 to mediate cancer-cell survival and inhibit antitumor T cell responses. *Nat Immunol* 2014;**15**:562−70.
30. Segers VFM, Dugaucquier L, Feyen E, Shakeri H, De Keulenaer GW. The role of ErbB4 in cancer. *Cell Oncol* 2020;**43**:335−52.
31. Qin YR, Tang H, Xie F, Liu H, Zhu Y, Ai J, et al. Characterization of tumor-suppressive function of SOX6 in human esophageal squamous cell carcinoma. *Clin Cancer Res* 2011;**17**:46−55.
32. Chen L, Xie Y, Ma X, Zhang Y, Li X, Zhang F, et al. SOX6 represses tumor growth of clear cell renal cell carcinoma by HMG domain-dependent regulation of Wnt/β-catenin signaling. *Mol Carcinog* 2020;**59**:1159−73.
33. Chen B, Dragomir MP, Yang C, Li Q, Horst D, Calin GA. Targeting non-coding RNAs to overcome cancer therapy resistance. *Signal Transduct Targeted Ther* 2022;**7**:121.
34. Zhao M, Wang R, Yang K, Jiang Y, Peng Y, Li Y, et al. Nucleic acid nanoassembly-enhanced RNA therapeutics and diagnosis. *Acta Pharm Sin B* 2023;**13**:916−41.
35. Wang M, Zhang L, Ren W, Li S, Zhi K, Zheng J, et al. Diagnostic value of circRNAs as potential biomarkers in oral squamous cell carcinoma: a meta-analysis. *Front Oncol* 2021;**11**:693284.
36. Zhang Y, Guo C, Yang S, Elkharti M, Liu R, Sun MZ, et al. NONHSAT021545/miR-330-3p/EREG: a cooperative axis in breast cancer prognosis and treatment. *J Clin Med* 2023;**12**:2478.

37. Wang X, Jian W, Luo Q, Fang L. CircSEMA4B inhibits the progression of breast cancer by encoding a novel protein SEMA4B-211aa and regulating AKT phosphorylation. *Cell Death Dis* 2022;**13**:794.
38. Yang C, Mou Z, Zhang Z, Wu S, Zhou Q, Chen Y, et al. Circular RNA RBPMS inhibits bladder cancer progression *via* miR-330-3p/RAI2 regulation. *Mol Ther Nucleic Acids* 2021;**23**:872−86.
39. Li Q, Wang W, Zhang M, Sun W, Shi W, Li F. Circular RNA circ-0016068 promotes the growth, migration, and invasion of prostate cancer cells by regulating the miR-330-3p/BMI-1 axis as a competing endogenous RNA. *Front Cell Dev Biol* 2020;**8**:827.
40. Wang J, Ke S, Gong Y, Cai Y, Xia L, Shi Z, et al. Circ_0011385 knockdown inhibits cell proliferation, migration and invasion, whereas promotes cell apoptosis by regulating miR-330-3p/MYO6 axis in colorectal cancer. *Biomed J* 2023;**46**:110−21.
41. Zhang G, Zhu Y, Jin C, Shi Q, An X, Song L, et al. CircRNA_0078767 promotes osteosarcoma progression by increasing CDK14 expression through sponging microRNA-330-3p. *Chem Biol Interact* 2022;**360**:109903.
42. Li H, Zheng D, Zhang B, Liu L, Ou J, Chen W, et al. Mir-208 promotes cell proliferation by repressing SOX6 expression in human esophageal squamous cell carcinoma. *J Transl Med* 2014;**12**:196.
43. Jiang W, Yuan Q, Jiang Y, Huang L, Chen C, Hu G, et al. Identification of Sox6 as a regulator of pancreatic cancer development. *J Cell Mol Med* 2018;**22**:1864−72.
44. Yu Y, Wang Z, Sun D, Zhou X, Wei X, Hou W, et al. miR-671 promotes prostate cancer cell proliferation by targeting tumor suppressor SOX6. *Eur J Pharmacol* 2018;**823**:65−71.
45. Zheng T, Wang W, Mohammadniaei M, Ashley J, Zhang M, Zhou N, et al. Anti-microRNA-21 oligonucleotide loaded spermine-modified acetalated dextran nanoparticles for B1 receptor-targeted gene therapy and antiangiogenesis therapy. *Adv Sci* 2022;**9**:e2103812.
46. Huang H, Han Q, Zheng H, Liu M, Shi S, Zhang T, et al. MAP4K4 mediates the SOX6-induced autophagy and reduces the chemosensitivity of cervical cancer. *Cell Death Dis* 2021;**13**:13.
47. Ghaferi M, Asadollahzadeh MJ, Akbarzadeh A, Ebrahimi Shahmabadi H, Alavi SE. Enhanced efficacy of pegylated liposomal cisplatin: *in vitro* and *in vivo* evaluation. *Int J Mol Sci* 2020;**21**:559.
48. Sindhwani S, Syed AM, Ngai J, Kingston BR, Maiorino L, Rothschild J, et al. The entry of nanoparticles into solid tumours. *Nat Mater* 2020;**19**:566−75.
49. Lei Z, Ding L, Yao C, Mo F, Li C, Huang Y, et al. A highly efficient tumor-targeting nanoprobe with a novel cell membrane permeability mechanism. *Adv Mater* 2019;**31**:e1807456.